

IEEE Copyright Notice

© 2025 IEEE.

Personal use of this material is permitted. Permission from IEEE must be obtained for all other uses, in any current or future media, including reprinting/republishing this material for advertising or promotional purposes, creating new collective works, for resale or redistribution to servers or lists, or reuse of any copyrighted component of this work in other works.

This file corresponds to the accepted version of the manuscript published in IEEE Robotics and Automation Letters, VOL. 11, NO. 1, pp. 282-289, JANUARY 2026. Digital Object Identifier 10.1109/LRA.2025.3632120

Continuous Gaussian Process Pre-Optimization for Asynchronous Event-Inertial Odometry

Zhixiang Wang, Xudong Li, Yizhai Zhang, Fan Zhang, and Panfeng Huang, *Senior Member, IEEE*

Abstract—Event cameras, as bio-inspired sensors, are asynchronously triggered with high-temporal resolution compared to intensity cameras. Recent work has focused on fusing the event measurements with inertial measurements to enable ego-motion estimation in high-speed and HDR environments. However, existing methods predominantly rely on IMU preintegration designed mainly for synchronous sensors and discrete-time frameworks. In this paper, we propose GPO, a continuous-time preintegration framework that can efficiently achieve tightly-coupled fusion of fully asynchronous sensors. Concretely, we model the preintegration as two local Temporal Gaussian Process (TGP) trajectories and leverage a light-weight two-step optimization to infer the continuous preintegration pseudo-measurements. We show that the Jacobians of arbitrary queried states can be naturally propagated using our framework, which enables GPO to be involved in the asynchronous fusion. Our method realizes a linear and constant time cost for optimization and query, respectively. To further validate the proposal, we leverage GPO to design an asynchronous event-inertial odometry and compare with other asynchronous fusion schemes. Experiments conducted on both public and own-collected datasets demonstrate that the proposed GPO offers significant advantages in terms of accuracy and efficiency, outperforming existing approaches in handling asynchronous sensor fusion. The code of GPO can be found at <https://github.com/NPU-RCIR/GPO-Preint>.

Index Terms—event-inertial fusion, Gaussian process regression, motion estimation, asynchronous fusion.

I. INTRODUCTION

The estimation of ego-motion is critical for robots to accomplish automated tasks, such as bridge inspection [1], disaster rescue [2], and autonomous driving [3]. Traditionally, this problem has been addressed by fusing various sensors using filter-based [4], optimization-based [5], or learning-based methods [6]. However, these conventional discrete-time estimation frameworks struggle with handling high-frequency or even asynchronous sensors effectively. To address this challenge, continuous-time methods have been proposed to associate measurements from different sensors with a unified, time-indexed trajectory, such as B-splines [7] or Temporal Gaussian Processes (TGP) [8].

Recent studies have demonstrated that event-inertial odometry based on continuous-time frameworks have great potential for ego-motion estimation in high-speed and High Dynamic Range (HDR) scenarios [9], [10]. Nonetheless, existing continuous-time event-inertial systems often involve

a substantial number of inertial factors and optimize them together with kinematic states of a global motion trajectory, leading to high computational consumption. Other schemes integrate inertial measurements (referred to as preintegration) between keyframes to reduce the number of inertial factors, but paying the cost of neglecting the rich motion information between integration intervals. Consequently, event factors can only rely on an imprecise prior trajectory to build re-projection relationships. Since the prior trajectory may violate the true motion, it can corrupt the estimation.

Continuous-time preintegration methods mitigate these issues by modeling the integration procedure as continuous inference using differential equations or latent states [11], [12]. This enables the asynchronous fusion ability to query on a local inertial preintegration trajectory. The primary drawback is that the initialization and inference are still time-consuming for online applications. In addition, the differential equation-based methods often have less supports for asynchronous querying and back-end optimization.

To address these challenges, we propose a hybrid estimation framework that combines the advantages of both discrete- and continuous-time methods. We introduce a continuous Gaussian Process pre-Optimization (GPO) framework to estimate the inertial preintegration pseudo-measurements. Our GPO employs a light-weight two-step optimization and achieves linear solving and constant query times, enabling precise kinematic state queries at arbitrary time. The asynchronous fusion ability of GPO is further validated by integrating it into an asynchronous event-inertial fusion system. Both the simulation and real-world experiments demonstrate the superior efficiency and accuracy performance of our method compared to state-of-the-art ones. In summary, the contributions of this paper are listed as below:

- 1) An efficient pre-optimization method that converts raw inertial measurements to continuous local TGP trajectory, enabling constant querying time at arbitrary time.
- 2) A Jacobian propagation strategy that enables adjustment of system states for any synchronous or asynchronous cost terms.
- 3) A complete asynchronous fusion pipeline for GPO, where the asynchronous fusion ability of GPO is validated by tightly-coupled fusion of event associations and inertial measurements at arbitrary timestamps.
- 4) Verification and analysis of the developed system on both public datasets and real-world experiments.

This work was supported by the National Natural Science Foundation of China under Grant Nos. 62573351 and 62022067. (*Corresponding author: Yizhai Zhang.*)

All authors are with Research Center for Intelligent Robotics, School of Astronautics, Northwestern Polytechnical University, Xi'an 710072, China (e-mail: wangzhixiang@mail.nwpu.edu.cn, zhangyizhai@nwpu.edu.cn).

II. RELATED WORK

A. Continuous-Time Estimation and Preintegration

The concept of preintegration was initially introduced by Lupton *et al.* [13] and Forster *et al.* [14]. Recently, Zhang *et al.* [15] utilized the discrete-time preintegration to a global TGP-based continuous-time fusion framework. However, it can only offer a relative motion measurement between two adjacent motion states, and ignores the contribution of high-frequency motion information for asynchronous sensor fusion. The discrete-time preintegration assumes constant measurements during each integration step, which may introduce additional errors. Differential equation-based methods [11], [16], [17] were designed to alleviate it by modeling the rigid motion using the kinematic formula. The Gaussian Process (GP)-based preintegration methods were proposed to model the IMU measurements as a group of latent states [18], [19]. But it only consider the 1-axis-rotation scenario and still rely on the iterative numerical integration. Further improvements were reported in LPM and GPM [20], [21] to model 3-axis rotation as latent states of three independent GPs. They further proposed GP-Preintegration (GPP) to support both attitude and translation preintegration by six independent GPs [12], where LPM is leveraged to finish initialization. Although their methods offer an asynchronous fusion capability, the high computational burden can degenerate the real-time performance. Recently, Burnett *et al.* [22], [23] modeled the raw IMU measurements as the direct observations of a global TGP trajectory. However, it introduced numerous inertial factors and thus requires high computational cost. Conversely, our proposal introduces the TGP theory into preintegration and suggests a two-step pre-optimization to instantiate a local TGP trajectory, which achieves superior efficiency.

B. Event-Inertial Odometry

Event-inertial odometry (EIO) has garnered significant attentions for its potential to estimate ego-motion in challenging scenarios [24]. Mahlkecht *et al.* [25] synchronized measurements from the Event-based KLT (EKLT) tracker [26] via extrapolation of fixed number of events and fused them with IMU data using a filter-based back-end. Rebecq *et al.* [27], [28] introduced a keyframe-based framework in which feature points from motion-compensated event frames are fused with discrete-time preintegration. Researchers also utilized Time Surface (TS) [29], which stores timestamps of most recent events at each pixel, to detect and track features using frame-based techniques [30], [31] and fuse them with discrete-time preintegration. In general, these methods transform asynchronous event streams into synchronous data associations and convert high-rate IMU data into inter-frame motion constraints through discrete-time preintegration. However, discrete-time estimation frameworks neglect the asynchronous nature of event cameras, resulting in suboptimal performance in challenging scenarios.

Event-triggered frameworks have been proposed to preserve the high-temporal resolution and asynchronous nature of event cameras. Liu *et al.* [32] introduced a monocular asynchronous back-end (without IMU) to trigger optimization by incoming

events. Wang *et al.* [10] developed a stereo event odometry using global TGP with an incremental back-end. Dai *et al.* [33] designed an event-inertial odometry where LPM was used to realize tightly-coupled fusion. Le *et al.* [34] extended this work by introducing a line feature tracker. Li *et al.* [35] realized asynchronous fusion of event-inertial odometry using GPP. Wang *et al.* [9] further extended this work by introducing a total asynchronous front-end and realized asynchronous fusion using various inertial schemes on global TGP. However, the initialization and query operators of the GPP are quite time-consuming. Moreover, the GPP initialized six independent GPs to fit the $SE(3)$ pose, which results in a sub-optimal attitude accuracy in practical EIO. Instead, the proposed GPO adopts two local TGP trajectories (on $SO(3)$ and \mathbb{R}^3) to model the continuous-time inertial preintegration, which handles the rotation Lie group more elegantly and achieves higher accuracy and efficiency in the real EIO system. Compared with global TGP-based methods [9], [23], our GPO excludes TGP states from the back-end optimization, thereby significantly reducing problem dimensionality.

III. METHODOLOGY

A. Inertial Preintegration

Define the measurements of the gyroscope and accelerometer be $\tilde{\omega}$ and \tilde{a} , respectively. The IMU's measurement model is as follows:

$$\begin{aligned}\tilde{\omega} &= \omega_b^{bi} + \mathbf{b}_g + \boldsymbol{\varsigma}_g, \\ \tilde{a} &= \mathbf{C}_{bi}(\ddot{\mathbf{r}}_i^{bi} - \mathbf{g}_i) + \mathbf{b}_a + \boldsymbol{\varsigma}_a,\end{aligned}\quad (1)$$

where $\boldsymbol{\varsigma}_g \sim \mathcal{N}(\mathbf{0}, \mathbf{Q}_g)$ and $\boldsymbol{\varsigma}_a \sim \mathcal{N}(\mathbf{0}, \mathbf{Q}_a)$ are the measurement noises, \mathbf{C}_{bi} the rotation matrix, \mathbf{r}_i^{bi} the translation, \mathbf{g}_i the gravitational acceleration, \mathbf{b}_g and \mathbf{b}_a the gyroscope and accelerometer biases. The observed value ω_b^{bi} represents the body (b -superscript) angular velocity with respect to inertial navigation frame (i -superscript) and expressed in body frame (b -subscript), and the body acceleration $\ddot{\mathbf{r}}_i^{bi}$ is the second time derivative of \mathbf{r}_i^{bi} . According to previous research [12], [14], the inertial preintegration pseudo-measurements in the time period $[t_n, t_{n+1}]$ can be expressed by

$$\begin{aligned}\Delta \mathbf{C} &= \prod_{t_n}^{t_{n+1}} \exp((\tilde{\omega}(\tau) - \mathbf{b}_g)d\tau), \\ \Delta \mathbf{v} &= \int_{t_n}^{t_{n+1}} \mathbf{C}_n(\tau)(\tilde{a}(\tau) - \mathbf{b}_a)d\tau, \\ \Delta \mathbf{r} &= \int_{t_n}^{t_{n+1}} \int_{t_n}^{\tau} \mathbf{C}_n(s)(\tilde{a}(s) - \mathbf{b}_a)dsd\tau,\end{aligned}\quad (2)$$

where τ and s indicate the timestamps, $\exp(): \mathbb{R}^3 \rightarrow SO(3)$ represents the exponential map, and $\Delta \mathbf{C} \in SO(3)$, $\Delta \mathbf{v} \in \mathbb{R}^3$, $\Delta \mathbf{r} \in \mathbb{R}^3$ is the rotation, linear velocity and translation components, respectively. As the multiplication is applied to compose on $SO(3)$, $\Delta \mathbf{C}$ uses the product integral. Note that $\mathbf{C}_n(\tau)$ is the rotation integral at time τ and can be computed from $\Delta \mathbf{C}$ simultaneously. When the estimated IMU biases \mathbf{b}_a and \mathbf{b}_g are changed, the inertial preintegration measurements in (2) are updated with linearized Jacobians.

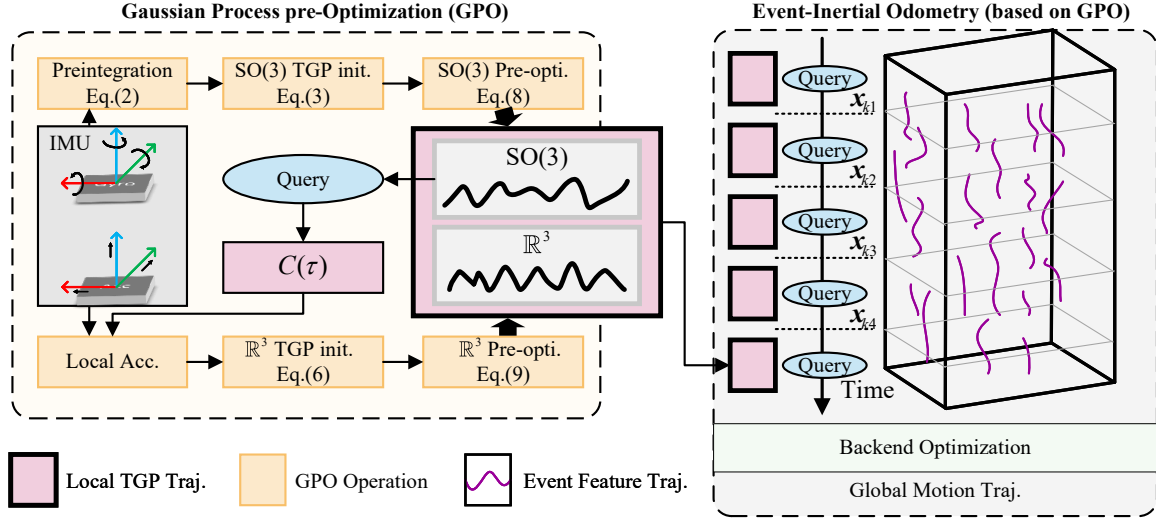


Fig. 1. System framework of the proposal. The GPO infers a local TGP-based trajectory during each pre-optimization (left part). The local trajectories, within the sliding-window of event-inertial odometry, will be queried by event feature trajectories to create asynchronous projection factors (right part).

B. GP Regression on Preintegration States

Although the inertial preintegration works well when applied in discrete-time visual-inertial system, it would be suboptimal for the asynchronous measurement fusion, such as the event-inertial odometry and incompatible frequency measurements of gyroscopes and accelerometers. We address this drawback by integrating a pre-optimization step, where raw inertial measurements are modeled as a local continuous-time trajectory (termed *pseudo-measurement trajectory*) using the sparse GP regression method.

Given the raw measurement $\tilde{\omega}(\tau_i)$ and $\tilde{\mathbf{a}}(\tau_j)$, $\tau_i, \tau_j \in [t_n, t_{n+1}]$, we expect to search the preintegration pseudo-measurements at arbitrary timestamp $\tau \in [t_n, t_{n+1}]$, even if the raw IMU measurements are asynchronous (i.e., $\tau_i \neq \tau_j$ when $i = j$ or $\tau_{i+1} - \tau_i \neq \tau_i - \tau_{i-1}$ or $\tau_{j+1} - \tau_j \neq \tau_j - \tau_{j-1}$). Assume the angular acceleration $\dot{\omega}(\tau)$ to obey a zero-mean GP. The differential equation for the rotation preintegration state can be defined as

$$\dot{C}(\tau) = C(\tau)(\omega(\tau))^\wedge, \quad \dot{\omega}(\tau) \sim \mathcal{GP}(\mathbf{0}, \mathbf{Q}_c \delta(\tau - \tau')), \quad (3)$$

where \wedge is the skew-symmetric operator, $\delta(\tau - \tau')$ is the Dirac delta function, and \mathbf{Q}_c is the power spectral density matrix [8]. Regarding the rotation preintegration ΔC in (2) as a continuous-time process, it can be described using the GP in (3) as

$$\begin{aligned} C(\tau) &= \mathbf{I} & \text{if } \tau = t_n, \\ C(\tau) &= \Delta C & \text{if } \tau = t_{n+1}, \\ \omega(\tau) &= \tilde{\omega}(\tau) - \mathbf{b}_g, \end{aligned} \quad (4)$$

where $\omega(\tau)$ is modeled as the bias corrected angular velocity. A local variable $\phi_k(\tau)$ is introduced to convert the nonlinear differential equation (3) to be a piece-wise linear one as

$$\begin{aligned} C_k(\tau) &= C_k \exp((\phi_k(\tau))^\wedge), \\ \ddot{\phi}_k(\tau) &\sim \mathcal{GP}(\mathbf{0}, \mathbf{Q}_c \delta(\tau - \tau')), \end{aligned} \quad (5)$$

where $C_k = C(\tau_k)$ is the linearization point and $C(\tau) \equiv C_k(\tau)$ is the rotation preintegration. The time derivative of

local variable has a relationship with the bias-corrected angular velocity as $\omega(\tau) = \mathcal{J}(\phi_k(\tau))\dot{\phi}_k(\tau)$, where $\mathcal{J}(\phi_k(\tau))$ is the right Jacobian of $\phi_k(\tau)$. In contrast, the state space equations for translation and velocity are inherently linear, defined as

$$\dot{\mathbf{r}}(\tau) = \mathbf{v}(\tau), \quad \dot{\mathbf{v}}(\tau) = \mathbf{a}(\tau), \quad \dot{\mathbf{a}}(\tau) \sim \mathcal{GP}(\mathbf{0}, \mathbf{Q}_r \delta(\tau - \tau')), \quad (6)$$

where $\mathbf{a}(\tau) = C_k(\tau)(\tilde{\mathbf{a}}(\tau) - \mathbf{b}_a)$ is a localized acceleration measurement (see Fig. 1 left part) corrected by the bias, and $\dot{\mathbf{a}}(\tau)$ is the ‘‘jerk’’ of the preintegration trajectory. As done in (4), we expect $\mathbf{r}(\tau) = \Delta \mathbf{r}$ and $\mathbf{v}(\tau) = \Delta \mathbf{v}$, when $\tau = t_{n+1}$. Both (5) and (6) have the similar closed-form solution as

$$\begin{aligned} \mathbf{x}_k(\tau) &= \mathbf{\Lambda}_k(\tau)\mathbf{x}_k(\tau_k) + \mathbf{\Psi}_k(\tau)\mathbf{x}_k(\tau_{k+1}), \\ \mathbf{\Lambda}_k(\tau) &= \mathbf{\Phi}(\tau, \tau_k) - \mathbf{\Psi}_k(\tau)\mathbf{\Phi}(\tau_{k+1}, \tau_k), \\ \mathbf{\Psi}_k(\tau) &= \mathbf{Q}_k(\tau)\mathbf{\Phi}(\tau_{k+1}, \tau)^\top \mathbf{Q}_k(\tau_{k+1})^{-1}, \end{aligned} \quad (7)$$

where $\mathbf{x}_k(\tau)$ is the local state variable, $\mathbf{\Phi}(\tau, t_k)$ the transition function, $\mathbf{Q}_k(\tau)$ the covariance matrix, and $\mathbf{\Lambda}_k(\tau)$ and $\mathbf{\Psi}_k(\tau)$ are the interpolation coefficients derived from $\mathbf{\Phi}(\tau, t_k)$ and $\mathbf{Q}_k(\tau)$. The detailed forms of $\mathbf{Q}_k(\tau)$ and $\mathbf{\Phi}(\tau, \tau_k)$ can be found in [35], [36]. In our context, the local state variables can be defined as $\gamma_k(\tau) \doteq [\phi_k(\tau), \dot{\phi}_k(\tau)]$ for (5), and $\mathbf{p}_k(\tau) \doteq [\mathbf{r}(\tau), \mathbf{v}(\tau), \mathbf{a}(\tau)]$ for (6), respectively. In fact, $\mathbf{p}_k(\tau) = \mathbf{p}(\tau)$ is a global state variable, we add subscript k for unifying the representation.

C. Two-step Pre-Optimization

Let $\tau_0 = t_n$ and $\tau_K = t_{n+1}$, we uniformly sample $K + 1$ points within the preintegration period $[t_n, t_{n+1}]$. The raw IMU measurements can be instantiated as a pseudo-measurement trajectory by estimating GP states at these sampled timestamps. Based on the foregoing pseudo-measurement model, two pre-optimization steps are adopt to infer this trajectory. Let the local TGP-based states for gyroscope preintegration be $\chi_k^g = [C_k, \omega_k]$, and for accelerometer preintegration be $\chi_k^a = [\mathbf{r}_k, \mathbf{v}_k, \mathbf{a}_k]$, where $k \in \{0, 1, \dots, K\}$. The objective

of pre-optimization, consisting of measurement residuals and GP prior residuals, can be defined as

$$\min_{\mathbf{x}_{k,k+1}^j} \sum_{i=0}^{M_g} \|e_g^i(\tau_k, \tau_{k+1})\|_{\mathbf{Q}_g}^2 + \sum_{k=0}^{K-1} \|e_c(\tau_k, \tau_{k+1})\|_{\mathbf{Q}_c^p}^2, \quad (8)$$

$$\min_{\mathbf{x}_{k,k+1}^j} \sum_{j=0}^{M_a} \|e_a^j(\tau_k, \tau_{k+1})\|_{\mathbf{Q}_a}^2 + \sum_{k=0}^{K-1} \|e_r(\tau_k, \tau_{k+1})\|_{\mathbf{Q}_r^p}^2, \quad (9)$$

where e_g^i , e_a^j indicates the related gyroscope (12) and accelerometer (13) measurement residuals in $[\tau_k, \tau_{k+1}]$, and e_c , e_r are the corresponding GP prior residuals as defined in (10) and (11), the covariance matrices \mathbf{Q}_c^p , \mathbf{Q}_r^p can be analytical inferred from \mathbf{Q}_c , \mathbf{Q}_r as done in [35], [36]. These problems are solved using GTSAM [9]. We use different subscripts $\{i, j, k\}$ to represent the possible asynchronism among raw measurements and estimated GP states. Based on the prior assumptions in (5), (6), the related prior residuals can be given by

$$e_c(\tau_k, \tau_{k+1}) = \begin{bmatrix} \Delta\tau_k \boldsymbol{\omega}_k - \log(\mathbf{C}_k^{-1} \mathbf{C}_{k+1}) \\ \boldsymbol{\omega}_k - \mathcal{J}(\log(\mathbf{C}_k^{-1} \mathbf{C}_{k+1}))^{-1} \boldsymbol{\omega}_{k+1} \end{bmatrix}, \quad (10)$$

$$e_r(\tau_k, \tau_{k+1}) = \begin{bmatrix} \Delta\tau_k \mathbf{v}_k + \frac{1}{2} \Delta\tau_k^2 \mathbf{a}_k - \mathbf{r}_{k,k+1} \\ \mathbf{v}_k + \Delta\tau_k \mathbf{a}_k - \mathbf{v}_{k+1} \\ \mathbf{a}_k - \mathbf{a}_{k+1} \end{bmatrix}, \quad (11)$$

where $\Delta\tau_k = \tau_{k+1} - \tau_k$, and $\mathbf{r}_{k,k+1} = \mathbf{r}(\tau_{k+1}) - \mathbf{r}(\tau_k)$. Since we have defined the relationship between GP states and raw IMU measurements in (4), (6), their corresponding residuals have concise forms as follows:

$$e_g^i(\tau_k, \tau_{k+1}) = \tilde{\boldsymbol{\omega}}(\tau_i) - \tilde{\mathbf{b}}_g - \boldsymbol{\omega}_k(\tau_i), \quad (12)$$

$$e_a^j(\tau_k, \tau_{k+1}) = \mathbf{C}_k(\tau_j)(\tilde{\mathbf{a}}(\tau_j) - \tilde{\mathbf{b}}_a) - \mathbf{a}_k(\tau_j), \quad (13)$$

where $\tau_k \leq \tau_i, \tau_j < \tau_{k+1}$. Note that $\boldsymbol{\omega}_k(\tau_i)$ is calculated by firstly interpolating the local state $\boldsymbol{\gamma}_k(\tau_i)$ using (7) and then $\boldsymbol{\omega}_k(\tau_i) = \mathcal{J}(\boldsymbol{\phi}_k(\tau_i))\dot{\boldsymbol{\phi}}_k(\tau_i)$. The rotation component $\mathbf{C}_k(\tau_j)$ is interpolated using (5), (7). According to the prior model, the pseudo-acceleration $\mathbf{a}_k(\tau_j)$ on the local TGP trajectory can be obtained from \mathbf{a}_k and \mathbf{a}_{k+1} by linear interpolation.

D. Event-Inertial Odometry

As shown in Fig. 1, an asynchronous event-inertial odometry is designed to validate the asynchronous fusion ability of GPO. We adopt the same asynchronous front-end as done in [9], but develop a different back-end for GPO. In our EIO, feature trajectories are tracked from raw event streams and inherently asynchronous with arbitrary timestamps. We leverage the proposed two-step pre-optimization to infer a series of local pseudo-measurement trajectories online. Then, they are fixed and involved in pseudo-measurement query and Jacobian propagation for asynchronous event projection factors. Both event projection and pseudo-measurement factors are tightly coupled in the back-end factor graph. Eventually, the expected motion states are estimated by solving the factor graph with a sliding-window optimizer.

For a given event projection factor occurring at an arbitrary timestamp, the residual Jacobians about neighbor estimated

pose and velocity can be analytically inferred with the queried pseudo preintegration measurement. The Jacobians about estimated biases need further consideration. The previous GPP method [12] calculates time-consuming numerical Jacobians of all latent states by extra integration steps. Instead, the proposed GPO memorizes the procedural Jacobians on timestamps of pseudo measurements using discrete-time formula and further propagates them to the arbitrary queried time using the Chain Rule. Assume $e_{ev}(\tau)$ be an asynchronous event projection residual, the Jacobians can be derived by

$$\frac{\partial e_{ev}(\tau)}{\partial \mathbf{b}(\tau)} = \frac{\partial e_{ev}(\tau)}{\partial \mathbf{x}(\tau)} \left(\frac{\partial \mathbf{x}(\tau)}{\partial \mathbf{x}(\tau_k)} \frac{\partial \mathbf{x}(\tau_k)}{\partial \mathbf{b}(\tau)} + \frac{\partial \mathbf{x}(\tau)}{\partial \mathbf{x}(\tau_{k+1})} \frac{\partial \mathbf{x}(\tau_{k+1})}{\partial \mathbf{b}(\tau)} \right), \quad (14)$$

where $\tau \in [\tau_k, \tau_{k+1}]$ is the projection timestamp, and $\mathbf{x}(\tau_k)$ and $\mathbf{x}(\tau_{k+1})$ are two nearest neighboring pseudo states, and $\mathbf{b}(\tau)$ is the bias variable. Normally, the Jacobian $\partial e_{ev}(\tau)/\partial \mathbf{x}(\tau)$ can be derived from the observation model, and the GP model of GPO can give $\frac{\partial \mathbf{x}(\tau)}{\partial \mathbf{x}(\tau_k)}$ analytically. The pseudo state $\mathbf{x}(\tau_k)$ is obtain by composing the last estimated state $\mathbf{x}(t_n)$ and later pseudo measurements $\Delta \mathbf{x}(\tau_k)$, i.e., $\mathbf{x}(\tau_k) = \mathbf{x}(t_n) \boxplus \Delta \mathbf{x}(\tau_k)$, where \boxplus is the plus operator for linear vectors and the matrix multiply for Lie group. Note that $\Delta \mathbf{x}(\tau_k) = \{\boldsymbol{\chi}_k^g, \boldsymbol{\chi}_k^a\}$ has been previously estimated in (8)-(9), and then used as a pseudo measurement in the backend factor graph to estimate the system state $\mathbf{x}(t_n)$, as shown in Fig. 1. Similarly, the IMU bias is regarded as constant within the whole integration period $[t_n, t_{n+1}]$. Therefore, we have

$$\frac{\partial \mathbf{x}(\tau_k)}{\partial \mathbf{b}(\tau)} \approx \frac{\partial \mathbf{x}(\tau_k)}{\partial \Delta \mathbf{x}(\tau_k)} \frac{\partial \Delta \mathbf{x}(\tau_k)}{\partial \mathbf{b}(\tau_k)}, \quad (15)$$

in which the procedural Jacobian $\frac{\partial \Delta \mathbf{x}(\tau_k)}{\partial \mathbf{b}(\tau_k)}$ can be efficiently inferred when initializing the pseudo measurements just similarly as done in discrete-time preintegration.

IV. EXPERIMENTS

In the experiments, we compare the proposed GPO with two similar GP-based methods, LPM [21] and GPP [12], to evaluate their accuracy, robustness, and computational efficiency. Additionally, we evaluate the performance of our EIO system against state-of-the-art methods by testing on public datasets and real-world experiments.

A. Precision Comparison

1) *Preintegration Errors*: An IMU simulator [12] is developed to generate raw IMU measurements and ground truth with different motion patterns. Then, we randomly sample the measurements and integrate them using LPM, GPP, and our GPO with five different integration periods and repeat each evaluation for 100 trials. For fair comparison, we set the same Gaussian noise ($1 \times 10^{-5} m/s^2$ for accelerometer and $1 \times 10^{-5} rad/s$ for gyroscope) and zero bias for all six axes. The errors of preintegration are summarized in Fig. 2-A. We compare their $\Delta \mathbf{C}$, $\Delta \mathbf{v}$, $\Delta \mathbf{r}$ with the ground truth. The GPP achieves the highest accuracy in rotational integration across different durations. The proposed GPO consistently outperforms LPM in all scenarios, achieving superior accuracy, especially in velocity and position integration during fast motions over long durations.

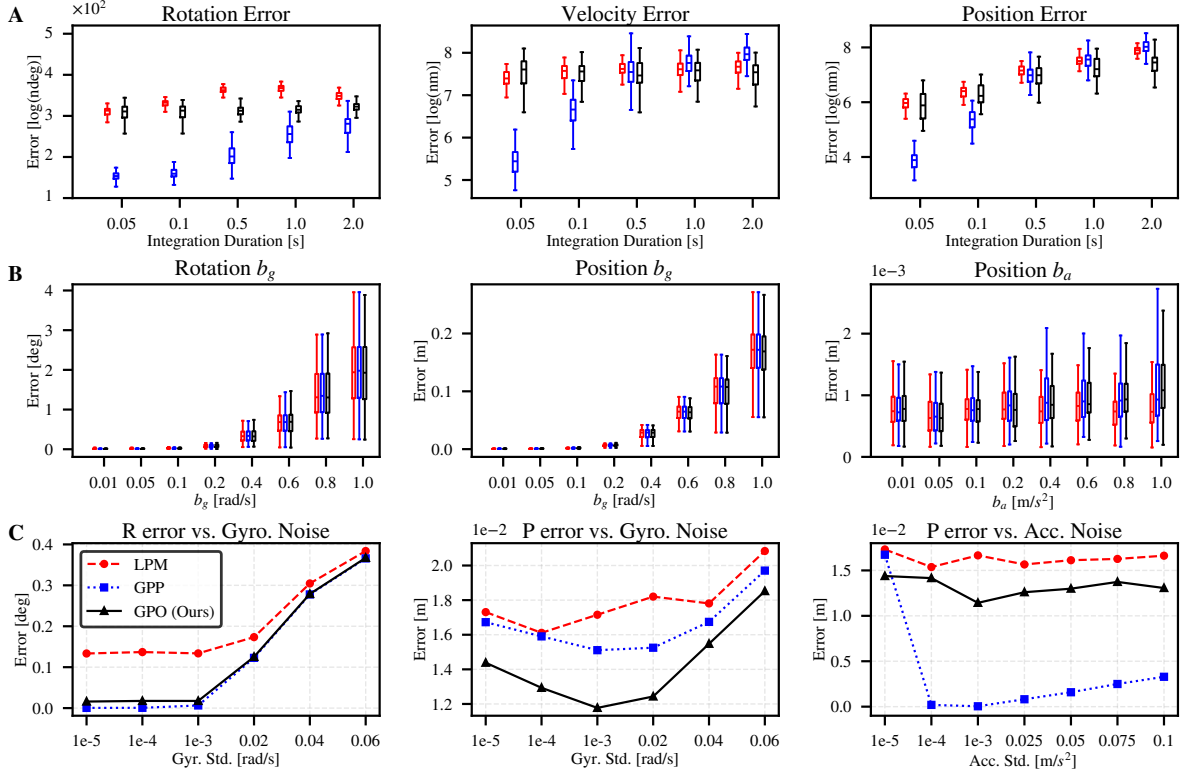


Fig. 2. Simulation evaluations of the proposed GPO. (A) Accuracy comparison under various integration durations. We randomly sample 100 trials and compare their ΔC , Δv , Δr with the ground truth for each integration period. (B) Procedural Jacobians evaluations. The Jacobian $\partial\Delta\mathbf{x}(\tau)/\partial\mathbf{b}(\tau)$ calculated using (14), (15) is adopted to correct the integration results of known biases, and compared with the reintegration results. Ten interpolation times τ are randomly sampled within the integration duration, with 100 trials per evaluation. (C) Robustness evaluations. Raw IMU measurements are contaminated with Gaussian noise of varying magnitudes. (0.5 s, 100 Hz).

2) *Jacobian Errors*: The Jacobians of preintegration results with respect to IMU bias $\frac{\partial\Delta\mathbf{x}(\tau)}{\partial\mathbf{b}(\tau)}$ are calculated using (14) and (15). It is employed to estimate bias updates and to refine the integration results within fusion systems. Intuitively, accurate Jacobians would lead to improved estimation results. For evaluation, the ground-truth biases and the Jacobians from various methods are used to correct the preintegration results, which are then compared to the reintegration results obtained with the known biases. Ten interpolation times τ are randomly sampled within the integration duration, and each evaluation is conducted over 100 trials. As shown in Fig. 2-B, the proposed approximate method (see Sec. III-D) achieves competitive results in all cases.

3) *Robustness against Noise*: Inevitably, real IMU sensors contain varying degrees of noise. Therefore, robustness to noise is a crucial criterion for evaluating the performance of a preintegration method. To this end, we designed different noise levels in the simulator and calculated the preintegration errors under two motion patterns. The results are shown in Fig. 2-C. All three methods exhibit comparable sensitivity to noise for slow motion. However, when applied to fast motion, GPO and GPP demonstrate superior noise robustness. Notably, under varying gyroscope noise levels, our GPO achieves lower positional integration errors compared to GPP, indicating enhanced robustness.

B. Time-Complexity Comparison

We summarize the time costs of preintegration and query, respectively. For each repeated integration trial (100 trials), 10 time points are randomly sampled within the integration duration, and the query operation is performed to compute the preintegrated quantities $\{\Delta C(\tau), \Delta v(\tau), \Delta r(\tau)\}$, along with the associated Jacobians and covariance. All computational efficiency evaluations are conducted on a desktop computer with an Intel Xeon Gold 6248R@4GHz, running Ubuntu 20.04 LTS. The experiments utilized only CPU resources without GPU or other parallel acceleration for the sake of fairness. The results are displayed in Fig. 3. The integration operation of the LPM resembles discrete-time preintegration and demonstrates the lowest computational cost (top, blue dashed line). Although the proposed GPO involves a two-step optimization process, it maintains high efficiency, with the computational time increasing linearly as the integration duration grows (top, green solid line). In contrast, the GPP is the most computationally expensive approach, characterized by a cubic time complexity (top, red dotted line). Furthermore, its computation time becomes increasingly unstable as the integration duration grows (top, red shaded area). Notably, our GPO achieves the best constant computational cost for querying pseudo-measurements, Jacobians, and covariance matrices (bottom, green solid line). This property makes GPO

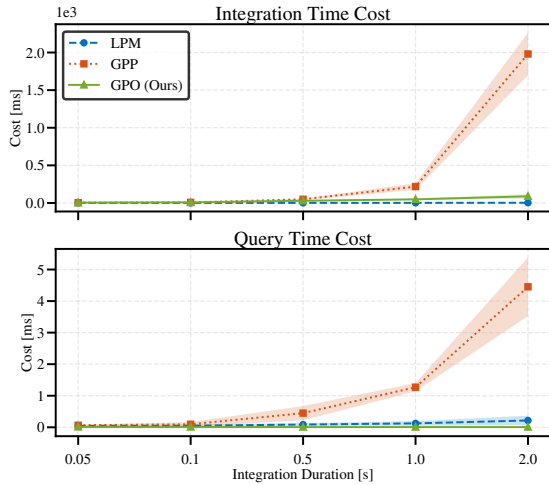


Fig. 3. Time cost comparison. Top: Preintegration time - LPM is fastest (blue dashed), GPO scales linearly (green solid), GPP has cubic complexity and becomes unstable with longer durations (red dotted, with shadow showing instability). Bottom: Query time - GPO achieves constant time for pseudo-measurements, Jacobians and covariance matrices (green solid), outperforming alternatives.

particularly well-suited for fusing high-temporal-resolution measurements from other asynchronous sensors.

C. Event-Inertial Odometry Application

Beyond preintegration evaluation, we introduce a dedicated event-inertial odometry system, where motion trajectories are inferred solely from fully asynchronous event associations and inertial measurements, in order to validate the asynchronous fusion capability of the proposed GPO. We incorporate GPP and global TGP into the same framework for a fair comparison. The detailed description can be found in [9], [12]. Our event-inertial odometry system leverages a similar initialization procedure as in [9]. The asynchronous feature trajectories are first sampled at a fixed frequency of 20 Hz. At each sampling timestamp, we interpolate the pixel coordinates between adjacent feature points to ensure precise temporal alignment. This procedure effectively converts the asynchronous initialization problem into a synchronous one. Subsequently, the visual-inertial initialization method [37] is employed to obtain initial estimates of pose, linear velocity, and bias. Finally, the complete asynchronous feature trajectories are incorporated into a full optimization to further refine the initial states and landmarks.

1) *Results for public datasets:* Our event-inertial odometry is compared with state-of-the-art monocular methods, including Ultimate-SLAM (USLAM) [28], DEVO [6], and PLEVIO [38], as well as stereo methods, including ESVIO (labeled as ESIO, E+I) [39], ESVIO+IMU [40], and ESVO2 [41]. To validate GPO in high-speed, aggressive, and HDR scenarios, we select DAVIS240C (DAVIS) [42], UZH-FPV (FPV) [43], VECtor [44] and HKU-Stereo (HKU-S) [39] datasets. These datasets contain both monocular and stereo event and inertial measurements, captured by high-speed flying drones and hand-held devices with rapid shaking and rotation.

TABLE I
THE COMPARATIVE RESULTS WITH MONOCULAR METHODS

Dataset	Sequence	USLAM [28]	DEVO [6]	PLEVIO [38]	TGP [9]	GPP [34]	GPO (Ours)
		C_{rmse} / MPE	C_{rmse} / MPE	C_{rmse} / MPE	C_{rmse} / MPE	C_{rmse} / MPE	C_{rmse} / MPE
DAVIS	boxes_6	7.45 / 0.41	66.68 / 0.73	- / 0.21	3.97 / 0.39	26.36 / 0.61	9.02 / 0.34
	boxes_t	15.67 / 0.37	3.40 / 0.06	- / 0.06	9.72 / 0.20	15.35 / 0.37	10.15 / 0.28
	poster_6	3.70 / 0.24	138.64 / 0.47	- / 0.14	5.20 / 0.40	37.96 / 0.75	5.30 / 0.30
	poster_t	6.07 / 0.25	2.67 / 0.06	- / 0.54	1.57 / 0.14	7.86 / 0.26	4.19 / 0.21
	dynam_6	5.79 / 0.34	4.28 / 0.09	- / 0.48	1.12 / 0.29	1.46 / 0.23	0.75 / 0.11
	dynam_t	17.43 / 1.00	3.64 / 0.09	- / 0.24	1.12 / 0.16	1.45 / 0.14	0.97 / 0.06
	hdr_bo	2.18 / 0.45	3.83 / 0.07	- / 0.10	2.33 / 0.31	39.12 / 0.60	7.56 / 0.34
	hdr_po	4.65 / 0.31	16.41 / 0.22	- / 0.12	1.53 / 0.28	3.30 / 0.19	6.83 / 0.19
Avg.	7.87 / 0.42	29.94 / 0.22	- / 0.24	3.32 / 0.27	16.61 / 0.40	5.60 / 0.23	
FPV	in_45_2	X / X	5.39 / 0.89	- / -	3.45 / 0.91	1.88 / 0.77	2.70 / 0.60
	in_45_4	- / 9.79	2.41 / 0.39	- / -	1.06 / 1.07	0.97 / 0.40	1.87 / 0.37
	in_45_9	- / 4.74	17.60 / 1.23	- / -	3.18 / 0.92	4.75 / 0.74	4.24 / 0.61
	in_for_9	X / X	1.95 / 0.53	- / 0.44	3.59 / 1.56	4.57 / 1.18	4.13 / 1.05
	in_for_10	X / X	2.01 / 0.48	- / 1.06	2.04 / 0.91	3.97 / 0.63	1.75 / 0.70
	Avg.	- / 7.27	5.87 / 0.70	- / 0.75	2.66 / 1.07	3.23 / 0.74	2.94 / 0.67

Units: [%] for MPE, [deg] for C_{rmse} , MPE is the Mean Position Error. The $SIM(3)$ alignment is applied to the estimated trajectory of DEVO, whereas the $SE(3)$ alignment is used for other event-inertial methods to ensure a fair comparison. C_{rmse} is the Root Mean Square Error of attitude matrices. The bold colored numbers indicate the best precision performance among the compared methods (orange for the best MPE, green for the best C_{rmse}), while underlined and bold black numbers denote the second-best precision. "X" represents that the particular method fails in a sequence, and "-" means the corresponding value is unavailable. It is noteworthy that the results of all methods except PLEVIO are reproduced using their open-source codes, which may lead to discrepancies compared to the results reported in their original papers. Each evaluation was repeated more than ten times, and the best results were selected to minimize the impact of random fluctuations.

The DSEC [45] dataset is selected to validate the performance in large-scale environments. For fair comparisons, we align the scale of monocular methods when comparing them with stereo systems. The scale of DEVO is also corrected when compared with our event-inertial odometry. The Mean Position Error (MPE) and the Root Mean Square Error of rotation angles C_{rmse} are evaluated as error metrics to quantify the position and attitude errors of the estimated trajectories. For example, MPE=0.88 % represents the mean position error would be 0.88 m when the total trajectory length is 100 m. The estimated results are summarized in Table I and II. Our GPO achieves second best position and attitude accuracy on the DAVIS240C dataset. The high accuracy of DEVO may benefit from the precise tracking of its learning-based frontend and the use of $SIM(3)$ alignment. However, for the ultra-high-speed sequences in the UZH-FPV (labeled as FPV in Table I) dataset, the voxel grids used by DEVO can become degenerate due to motion blur. In contrast, our GPO-based pipeline achieves the best performance through high-temporal-resolution tracking and fully asynchronous fusion. USLAM (E+I) fails in most high-speed sequences, whereas PLEVIO (E+F+I) maintains its accuracy through the incorporation of intensity frames and line features. As shown in Table II, our asynchronous monocular pipeline demonstrates best accuracy in most sequences of VECtor and HKU-Stereo datasets. Although the position accuracy may be facilitated by scale alignment, our method outperforms the compared stereo methods in terms of robustness under aggressive scenarios. For the large scale sequences of DSEC, the TGP-based pipeline obtains the highest precision in both attitude and position estimation. This is mainly attributed to the use of the White-Noise-on-Jerk (WNOJ) prior. Since these sequences are captured using a car moving at nearly constant velocity with smooth rotations, the motion patterns closely align with the assumptions of the WNOJ model.

2) *Results for own-collected data:* The DVXplorer (640 × 480 pixels) event camera is mounted to a DJI M300 quadrotor (see Fig. 4). The event streams of camera and the inertial measurements of the quadrotor are simultaneously collected together with ground truth. Ground truth is provided by an Optitrack motion capture system for indoor sequences and

TABLE II
THE COMPARATIVE RESULTS WITH STEREO METHODS

Dataset	Sequence	ESIO [39]	ESVO+IMU [40]	ESVO2 [41]	TGP [9]	GPP [34]	GPO (Ours)
		C_{rmse} / MPE	C_{rmse} / MPE	C_{rmse} / MPE	C_{rmse} / MPE	C_{rmse} / MPE	C_{rmse} / MPE
DSEC	city_04_a	4.83 / 4.33	3.99 / 0.38	3.62 / 0.23	1.87 / 0.58	3.91 / 3.59	6.75 / 2.65
	city_04_b	10.08 / 6.02	3.65 / 0.91	2.90 / 1.24	1.33 / 0.06	19.89 / 0.05	26.49 / 0.03
	city_04_c	4.52 / 1.59	16.29 / 1.07	7.40 / 0.84	2.85 / 0.96	2.16 / 0.47	2.09 / 0.22
	city_04_d	12.03 / 11.03	26.12 / 1.20	19.95 / 0.86	10.13 / 0.20	10.70 / 0.45	11.03 / 0.21
	city_04_e	19.42 / 11.74	13.51 / 0.82	7.33 / 0.42	1.15 / 0.27	2.89 / 0.03	4.26 / 0.03
	city_04_f	32.62 / 9.02	6.39 / 1.19	12.09 / 0.50	7.56 / 0.47	3.18 / 0.11	3.29 / 0.20
Avg.	13.92 / 7.29	11.66 / 0.92	8.88 / 0.68	4.15 / 0.42	7.12 / 0.78	8.99 / 0.56	
VECTer	desk_fl	6.60 / 4.67	X / X	X / X	18.72 / 1.23	17.19 / 0.87	6.74 / 0.74
	hdr_fl	X / X	X / X	X / X	4.65 / 0.72	6.86 / 0.92	4.38 / 0.62
	mount_fl	X / X	X / X	X / X	5.77 / 0.33	4.94 / 0.41	3.24 / 0.23
	robot_fl	X / X	X / X	X / X	9.30 / 1.07	3.83 / 0.62	1.67 / 0.42
	sofa_fl	X / X	X / X	X / X	10.78 / 0.73	11.38 / 0.68	6.61 / 0.45
	Avg.	6.60 / 4.67	- / -	- / -	9.84 / 0.82	8.84 / 0.70	4.53 / 0.49
HKU-S	agg_bip	20.10 / 3.40	X / X	X / X	10.29 / 1.11	9.21 / 0.81	7.92 / 0.64
	agg_rot	28.43 / 0.83	X / X	X / X	9.30 / 0.16	7.28 / 0.19	1.88 / 0.23
	agg_tran	17.53 / 0.57	X / X	X / X	7.73 / 0.22	6.87 / 0.19	4.89 / 0.19
	hdr_agg	18.52 / 1.44	X / X	X / X	22.24 / 0.60	10.68 / 0.48	19.46 / 0.55
	hdr_circle	13.95 / 0.50	X / X	X / X	7.94 / 0.49	6.93 / 0.85	6.01 / 0.32
	hdr_tran_rot	23.85 / 0.95	X / X	X / X	1.84 / 0.30	6.65 / 0.45	7.35 / 0.41
Avg.	20.40 / 1.28	- / -	- / -	9.89 / 0.48	8.10 / 0.50	7.92 / 0.39	

Units: [%] for MPE, [deg] for C_{rmse} . MPE is the Mean Position Error where the $SE(3)$ transformation is used to align the estimated trajectory and ground truth for stereo methods, while the $SI(3)$ transformation is leveraged to align estimated trajectories of monocular methods. The results for ESIO, ESVO+IMU, and ESVO2 on the DSEC dataset are obtained using their public available raw trajectories, while other unavailable results are reproduced using their source codes with recommended parameters and configurations.

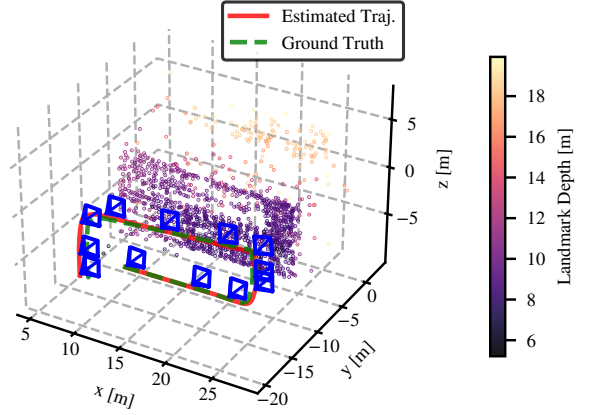


Fig. 5. Estimated trajectory and landmarks for outdoor_05.

TABLE III
THE RMSE OF OWN-COLLECTED DATA

Sequence	USLAM [28]		TGP [9]		GPP [34]		GPO (Ours)	
	C_{rmse}	MPE	C_{rmse}	MPE	C_{rmse}	MPE	C_{rmse}	MPE
indoor_02	7.16	2.83	6.30	1.15	6.51	1.38	2.90	0.86
indoor_03	98.18	5.47	4.08	0.85	5.07	2.03	2.32	1.02
outdoor_01	9.87	4.50	2.66	2.30	0.73	2.47	0.53	2.15
outdoor_02	X	X	1.64	0.37	1.47	1.05	0.74	0.92
outdoor_03	X	X	1.03	0.45	0.61	0.15	0.49	0.15
outdoor_05	11.11	2.92	3.37	1.80	6.44	2.37	1.60	1.12
outdoor_06	17.60	8.36	1.50	0.32	3.28	0.46	1.64	0.54
Avg.	-	-	2.94	1.03	3.44	1.42	1.46	0.97

Units: [%m] for MPE, [deg] for C_{rmse} . All methods are aligned with the ground truth using the position and yaw angle transformation.

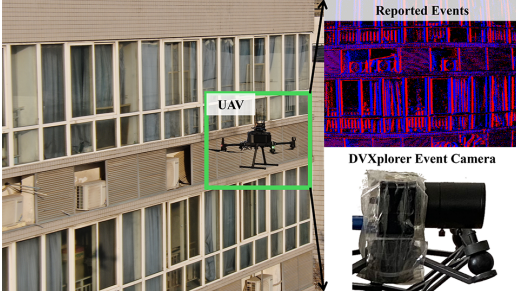


Fig. 4. Real-world experiment scenario.

by Real-Time Kinematic (RTK) for outdoor scenarios. The quadrotor mainly executes aggressive translational motion, which means the baseline trajectories have smaller variations in yaw angles, as displayed in Fig. 5. The roll and pitch variations are mainly caused by the acceleration of the drone. As shown in Table III, our GPO-based method outperforms the others in both attitude and position estimation. Compared with global TGP, GPO improves the position and attitude accuracy by 5.83% and 50.34%. Intuitively, the GPO can be regarded as a low-pass filter for the noisy inertial measurements, thereby it can reduce the accidental measurement errors in raw measurements. Otherwise, its continuous-time integration model can normally achieve higher accuracy than discrete-time preintegration. In summary, the GPO will become a more efficient and precise candidate for fusing totally asynchronous measurements with IMU.

TABLE IV
THE RUNTIME COMPARISON OF EACH MODULE

Sequence	Method	Front-End	Preintegration	Construct Factors	Optimization
dynam_6	GPP	3.17×10^{-3}	7.44	21.54	826.52
	GPO		14.33	13.68	461.15
desk_fl	GPP	5.82×10^{-3}	0.89	7.70	292.81
	GPO		1.73	7.37	240.52
hdr_circle	GPP	4.01×10^{-3}	7.33	12.76	452.48
	GPO		11.30	5.87	375.85

Units: [ms/event] for the asynchronous Front-end, [ms] for other modules. Bold numbers indicate higher time efficiency.

3) *Efficiency Analysis of the Odometry System:* To assess the time efficiency of the GPO method in practical odometry systems, the computational breakdown for each module is recorded and compared with the GPP-based odometry. Since the asynchronous front-end processes raw event streams in an event-by-event manner, the average processing time per event, rather than per frame, is reported, as shown in Table IV. Despite the time cost being reduced to μs magnitude, the serial processing still introduces a time lag that is roughly two times the real-time requirement. As our GPO obtains constant time cost for querying pseudo-states, the GPO-based method achieves superior time efficiency for constructing factor graph and back-end optimization, as in Table IV. The higher integration efficiency of GPP primarily results from the segmented parallel solving strategy during testing. A similar approach could be adopted for GPO in the future to further enhance its integration performance.

V. CONCLUSION

In this study, we proposed GPO, an efficient local TGP-based preintegration method specially designed for asynchronous fusion. We evaluated its performance against other GP-based methods, LPM, GPP, and global TGP. The experimental results demonstrate that GPO effectively balances accuracy, robustness, and computational efficiency. GPO achieves a constant time cost for querying pseudo-measurements, Jacobians, and covariance matrices, and linear cost for preintegration. The local pre-optimization can reduce the complexity of back-end optimization and improve the estimation accuracy. Therefore, we suggest the GPO be a new optional scheme for asynchronous sensor fusion.

REFERENCES

- [1] Z. Wang, X. Li, Y. Zhang, and P. Huang, "Localization, planning, and control of a uav for rapid complete coverage bridge inspection in large-scale intermittent gps environments," *IEEE Trans. Control Syst. Technol.*, vol. 32, no. 4, pp. 1357–1369, 2024.
- [2] A. Albanese, V. Sciancalepore, and X. Costa-Pérez, "Sardo: An automated search-and-rescue drone-based solution for victims localization," *IEEE Trans. Mobile Comput.*, vol. 21, no. 9, pp. 3312–3325, 2021.
- [3] H. Li, Y. Duan, X. Zhang, H. Liu, J. Ji, and Y. Zhang, "Occ-vo: Dense mapping via 3d occupancy-based visual odometry for autonomous driving," in *Proc. IEEE Int. Conf. Robot. Autom.* IEEE, 2024, pp. 17961–17967.
- [4] A. Fornasier, P. van Goor, E. Allak, R. Mahony, and S. Weiss, "Msceqf: A multi state constraint equivariant filter for vision-aided inertial navigation," *IEEE Robot. Autom. Lett.*, vol. 9, no. 1, pp. 731–738, 2023.
- [5] Y. Zhang, J. Xu, P. Zhang, W. Li, K. Yu, and P. Huang, "Monocular visual-inertial sensing of unknown rotating objects: Observability analyses and case study for metric 3d reconstructing of space debris," *IEEE Robot. Autom. Lett.*, vol. 7, no. 2, pp. 2423–2430, 2022.
- [6] S. Klenk, M. Motzet, L. Koestler, and D. Cremers, "Deep event visual odometry," in *Proc. Int. Conf. 3D Vision.* IEEE, 2024, pp. 739–749.
- [7] J. Lv, X. Lang, J. Xu, M. Wang, Y. Liu, and X. Zuo, "Continuous-time fixed-lag smoothing for lidar-inertial-camera slam," *IEEE/ASME Trans. Mechatronics*, vol. 28, no. 4, pp. 2259–2270, 2023.
- [8] W. Talbot, J. Nubert, T. Tuna, C. Cadena, F. Dümbsgen, J. Tordesillas, T. D. Barfoot, and M. Hutter, "Continuous-time state estimation methods in robotics: A survey," *arXiv preprint arXiv:2411.03951*, 2024.
- [9] Z. Wang, X. Li, Y. Zhang, F. Zhang, and P. Huang, "Asyneio: Asynchronous monocular event-inertial odometry using gaussian process regression," *IEEE Trans. Robot.*, vol. 41, pp. 5020–5039, 2025.
- [10] J. Wang and J. D. Gammell, "Event-based stereo visual odometry with native temporal resolution via continuous-time gaussian process regression," *IEEE Robot. Autom. Lett.*, vol. 8, no. 10, pp. 6707–6714, 2023.
- [11] K. Eickenhoff, P. Geneva, and G. Huang, "High-accuracy preintegration for visual-inertial navigation," in *Proc. Algorithmic Found. Robot. XII.* Springer, 2020, pp. 48–63.
- [12] C. Le Gentil and T. Vidal-Calleja, "Continuous latent state preintegration for inertial-aided systems," *Int. J. Robot. Res.*, vol. 42, no. 10, pp. 874–900, 2023.
- [13] T. Lupton and S. Sukkariéh, "Visual-inertial-aided navigation for high-dynamic motion in built environments without initial conditions," *IEEE Trans. Robot.*, vol. 28, no. 1, pp. 61–76, 2011.
- [14] C. Forster, L. Carlone, F. Dellaert, and D. Scaramuzza, "Imu preintegration on manifold for efficient visual-inertial maximum-a-posteriori estimation," in *Proc. Robot. Sci. Syst.*, 2015.
- [15] H. Zhang, C.-C. Chen, H. Vallery, and T. D. Barfoot, "Gnss/multi-sensor fusion using continuous-time factor graph optimization for robust localization," *IEEE Trans. Robot.*, vol. 40, pp. 4003–4023, 2024.
- [16] S. Shen, N. Michael, and V. Kumar, "Tightly-coupled monocular visual-inertial fusion for autonomous flight of rotorcraft mavs," in *Proc. IEEE Int. Conf. Robot. Autom.* IEEE, 2015, pp. 5303–5310.
- [17] K. Eickenhoff, P. Geneva, and G. Huang, "Closed-form preintegration methods for graph-based visual-inertial navigation," *Int. J. Robot. Res.*, vol. 38, no. 5, pp. 563–586, 2019.
- [18] C. Le Gentil, T. Vidal-Calleja, and S. Huang, "Gaussian process preintegration for inertial-aided state estimation," *IEEE Robot. Autom. Lett.*, vol. 5, no. 2, pp. 2108–2114, 2020.
- [19] C. Le Gentil, T. Vidal-Calleja, and S. Huang, "3d lidar-imu calibration based on upsampled preintegrated measurements for motion distortion correction," in *Proc. IEEE Int. Conf. Robot. Autom.* IEEE, 2018, pp. 2149–2155.
- [20] C. Le Gentil, T. Vidal-Calleja, and S. Huang, "In2laama: Inertial lidar localization autocalibration and mapping," *IEEE Trans. Robot.*, vol. 37, no. 1, pp. 275–290, 2020.
- [21] C. Le Gentil and T. Vidal-Calleja, "Continuous integration over so (3) for imu preintegration," in *Proc. Robot.: Sci. Syst.*, 2021.
- [22] X. Zheng and J. Zhu, "Traj-lio: A resilient multi-lidar multi-imu state estimator through sparse gaussian process," *arXiv preprint arXiv:2402.09189*, 2024.
- [23] K. Burnett, A. P. Schoellig, and T. D. Barfoot, "Continuous-time radar-inertial and lidar-inertial odometry using a gaussian process motion prior," *IEEE Trans. Robot.*, vol. 41, pp. 1059–1076, 2024.
- [24] G. Gallego, T. Delbrück, G. Orchard, C. Bartolozzi, B. Taba, A. Censi, S. Leutenegger, A. J. Davison, J. Conradt, K. Daniilidis et al., "Event-based vision: A survey," *IEEE Trans. Pattern Anal. Mach. Intell.*, vol. 44, no. 1, pp. 154–180, 2020.
- [25] F. Mahlknecht, D. Gehrig, J. Nash, F. M. Rockenbauer, B. Morrell, J. Delaune, and D. Scaramuzza, "Exploring event camera-based odometry for planetary robots," *IEEE Robot. Autom. Lett.*, vol. 7, no. 4, pp. 8651–8658, 2022.
- [26] D. Gehrig, H. Rebecq, G. Gallego, and D. Scaramuzza, "Ekl: Asynchronous photometric feature tracking using events and frames," *Int. J. Comput. Vis.*, vol. 128, no. 3, pp. 601–618, 2020.
- [27] H. Rebecq, T. Horstschaefer, and D. Scaramuzza, "Real-time visual-inertial odometry for event cameras using keyframe-based nonlinear optimization," in *Proc. Brit. Mach. Vis. Conf.*, Sep. 2017, pp. 1–12.
- [28] A. R. Vidal, H. Rebecq, T. Horstschaefer, and D. Scaramuzza, "Ultimate slam? combining events, images, and imu for robust visual slam in hdr and high-speed scenarios," *IEEE Robot. Autom. Lett.*, vol. 3, no. 2, pp. 994–1001, 2018.
- [29] X. Lagorce, G. Orchard, F. Galluppi, B. E. Shi, and R. B. Benosman, "Hots: a hierarchy of event-based time-surfaces for pattern recognition," *IEEE Trans. Pattern Anal. Mach. Intell.*, vol. 39, no. 7, pp. 1346–1359, 2016.
- [30] W. Guan and P. Lu, "Monocular event visual inertial odometry based on event-corner using sliding windows graph-based optimization," in *Proc. IEEE/RSJ Int. Conf. Intell. Robot. Syst.* IEEE, 2022, pp. 2438–2445.
- [31] K. Tang, X. Lang, Y. Ma, Y. Huang, L. Li, Y. Liu, and J. Lv, "Monocular event-inertial odometry with adaptive decay-based time surface and polarity-aware tracking," *arXiv preprint arXiv:2409.13971*, 2024.
- [32] D. Liu, A. Parra, Y. Latif, B. Chen, T.-J. Chin, and I. Reid, "Asynchronous optimisation for event-based visual odometry," in *Proc. IEEE Int. Conf. Robot. Autom.*, 2022, pp. 9432–9438.
- [33] B. Dai, C. Le Gentil, and T. Vidal-Calleja, "A tightly-coupled event-inertial odometry using exponential decay and linear preintegrated measurements," in *Proc. IEEE/RSJ Int. Conf. Intell. Robot. Syst.* IEEE, 2022, pp. 9475–9482.
- [34] C. Le Gentil, F. Tschopp, I. Alzugaray, T. Vidal-Calleja, R. Siegwart, and J. Nieto, "Idol: A framework for imu-dvs odometry using lines," in *Proc. IEEE/RSJ Int. Conf. Intell. Robot. Syst.* IEEE, 2020, pp. 5863–5870.
- [35] X. Li, Z. Wang, Y. Zhang, F. Zhang, and P. Huang, "Asynchronous event-inertial odometry using a unified gaussian process regression framework," in *Proc. IEEE/RSJ Int. Conf. Intell. Robot. Syst.* IEEE, 2024, pp. 7773–7778.
- [36] T. Y. Tang, D. J. Yoon, and T. D. Barfoot, "A white-noise-on-jerk motion prior for continuous-time trajectory estimation on se(3)," *IEEE Robot. Autom. Lett.*, vol. 4, no. 2, pp. 594–601, 2019.
- [37] T. Qin, P. Li, and S. Shen, "Vins-mono: A robust and versatile monocular visual-inertial state estimator," *IEEE Trans. Robot.*, vol. 34, no. 4, pp. 1004–1020, 2018.
- [38] W. Guan, P. Chen, Y. Xie, and P. Lu, "Pl-evio: Robust monocular event-based visual inertial odometry with point and line features," *IEEE Trans. Autom. Sci. Eng.*, vol. 21, no. 4, pp. 6277–6293, 2023.
- [39] P. Chen, W. Guan, and P. Lu, "Esvio: Event-based stereo visual inertial odometry," *IEEE Robot. Autom. Lett.*, vol. 8, no. 6, pp. 3661–3668, 2023.
- [40] J. Niu, S. Zhong, and Y. Zhou, "Imu-aided event-based stereo visual odometry," in *Proc. IEEE Int. Conf. Robot. Autom.* IEEE, 2024, pp. 11977–11983.
- [41] J. Niu, S. Zhong, X. Lu, S. Shen, G. Gallego, and Y. Zhou, "Esvo2: Direct visual-inertial odometry with stereo event cameras," *IEEE Trans. Robot.*, vol. 41, pp. 2164–2183, 2025.
- [42] E. Mueggler, H. Rebecq, G. Gallego, T. Delbruck, and D. Scaramuzza, "The event-camera dataset and simulator: Event-based data for pose estimation, visual odometry, and slam," *Int. J. Robot. Res.*, vol. 36, no. 2, pp. 142–149, 2017.
- [43] J. Delmerico, T. Cieslewski, H. Rebecq, M. Faessler, and D. Scaramuzza, "Are we ready for autonomous drone racing? the uzh-fpv drone racing dataset," in *Proc. IEEE Int. Conf. Robot. Autom.* IEEE, 2019, pp. 6713–6719.
- [44] L. Gao, Y. Liang, J. Yang, S. Wu, C. Wang, J. Chen, and L. Kneip, "Vector: A versatile event-centric benchmark for multi-sensor slam," *IEEE Robot. Autom. Lett.*, vol. 7, no. 3, pp. 8217–8224, 2022.
- [45] M. Gehrig, W. Aarents, D. Gehrig, and D. Scaramuzza, "Dsec: A stereo event camera dataset for driving scenarios," *IEEE Robot. Autom. Lett.*, vol. 6, no. 3, pp. 4947–4954, 2021.